Chinese Chemical Letters 33 (2022) 486–490

Contents lists available at ScienceDirect

Chinese Chemical Letters

journal homepage: www.elsevier.com/locate/cclet

# Mixed transition-metal oxides@carbon core-shell nanostructures derived from heterometallic clusters for enhanced lithium storage

Yanting Chu, Shenglin Xiong*

*School of Chemistry and Chemical Engineering, State Key Laboratory of Crystal Materials, Shandong University, Ji'nan 250100, China*

ARTICLE INFO

*Article history:*
Received 28 May 2021
Revised 24 June 2021
Accepted 27 June 2021
Available online 3 July 2021

*Keywords:*
$MFe_2O_4$
Core-shell nanoparticles
Heterometallic clusters
Anode
Lithium–ion batteries

ABSTRACT

Multicomponent binary metal oxide-involved hybrid structures with unique physicochemical properties have received extensive attention due to their fascinating electrochemical performance. Herein, a flexible strategy, which involves the preparation of dual-functional heterometallic $Fe_2M$ clusters and their subsequent sintering treatment, is developed to engineer novel 3D hierarchical porous structures assembled with $MFe_2O_4$ (M = Co, Mn, Ni and Zn) nanoparticles confined within carbon outer shell (denoted as $MFe_2O_4$@C HPSs). In this intriguing construction, it can be observed that $MFe_2O_4$@C HPSs comprised of carbon coated secondary $MFe_2O_4$ nanoparticles with an interconnected carbon network. The as-prepared $MFe_2O_4$@C HPSs possess combined advantages of high capacity of $MFe_2O_4$ and high conductivity of carbon. As expected, the $MFe_2O_4$@C HPSs offer a high reversible capacity, high cycling stability and superior rate performance. The interconnected conductive carbon shells facilitates fast ion and electron transport and accommodates the mechanical strain. In addition, nanosized $MFe_2O_4$ particles, which shorten the ion-transport path and provide extra electroactive sites, also improve the reaction kinetics. Moreover, these $MFe_2O_4$@C HPSs exhibit good structural integrity during repeated charging and discharging. The research perspective and strategy reported here are highly versatile and shed new light on the synthesis of other advanced electrode for various applications.



Transition metal oxides (TMOs), as a significant class of inorganic solid materials, have been widely investigated as electrode materials for energy storage devices including fuel cells, electrochemical capacitors (ECs), and lithium-ion batteries (LIBs) [1-7]. In particular, binary metal oxides with two different metal cations exhibit high electrochemical activities because of their complex chemical composition and the synergic effects of multiple metal species [8,9]. For example, spinel $CoFe_2O_4$ with a high theoretical capacity of 916 mAh/g, possesses much better electrical conductivity and hence has been considered as a promising anode material for LIBs [10-14]. However, it is difficult to synthesize multicomponent hybrid structures of binary metal oxides because different materials with unique physicochemical properties could not easily be contained simultaneously during the preparation process.

In recent years, metal–organic frameworks (MOFs) with diverse chemical compositions, designable topological architectures and well-defined structures are of enormous potential as an emerging class of well-ordered crystalline inorganic-organic hybrid porous materials for various applications [15-17]. Importantly, MOFs can be readily transformed to porous carbon-based composite materials with metal oxides, metal sulfides, and metal phosphides, which always exhibit incomparable properties with their single components [18-24]. Different from MOFs, metal-organic clusters (MOCs) are another kind of inorganic-organic hybrid materials featured with atom-precise structures, polynuclear metal atoms aggregations, uniform sizes, zero-dimensional and free-standing nature [25]. Notably, compared to polynuclear monometallic clusters, the heterometallic clusters (HMCs) are atom-precise molecular materials that have two or more than two kinds of metal atoms in one unity [26-28]. Different metal centers in one cluster can bring in novel molecular structure due to different coordination preferences, various metal ratios, as well as enhanced properties due to the synergistic interactions between them. More importantly, more kinds of metal centers could induce the formation of hybrid metal compositions, such as mixed metal oxides, metal doped metal oxides, even some interesting heterojunctions. In spite of considerable efforts on the preparation of various derivative hybrid materials from the corresponding MOFs [18-23], to the best of our knowledge, the dual-functional properties of MOCs especially HMCs are completely unexplored to date.

* Corresponding author.
*E-mail address:* chexsl@sdu.edu.cn (S. Xiong).

https://doi.org/10.1016/j.cclet.2021.06.074
1001-8417/

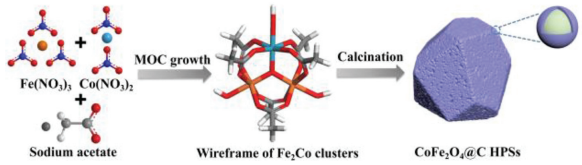


**Fig. 1.** Schematic illustration of the synthesis process of $CoFe_2O_4$@C HPSs.

Herein, for the first time, we report novel 3D hierarchical porous structures assembled with $MFe_2O_4$ (M = $CoFe_2O_4$, $MnFe_2O_4$, $NiFe_2O_4$ and $ZnFe_2O_4$) nanoparticles confined within carbon outer shell (denoted as $MFe_2O_4$@C HPSs) by using dual-functional heterometallic $Fe^{III}_2Co^{II}O(CH_3COO)_6(H_2O)_3{\cdot}2H_2O$ ($Fe_2M$) clusters as both sacrificial template and carbon source. Compared with other methods meanwhile requiring metal and carbon sources, $Fe_2M$ clusters include both of two components in one precursor. Fe and M atoms were homogenously distributed in three apexes of an equilateral triangle. Upon pyrolysis, the cleavage of C–O bond was transformed to carbon, while $Fe_2M$ cores were *in situ* transformed to uniform binary $MFe_2O_4$ nanoparticles, producing the final $MFe_2O_4$@C HPSs. In the as-obtained structure, uniform $MFe_2O_4$ nanoparticles are confined in the interconnected network of carbon shells and assemble into 3D porous hybrid structures. These porous hybrid structures possess good electrolyte diffusion in the pores and good electronic conductivity through the network-like carbon shell-layer. As expected, the as-synthesized $MFe_2O_4$@C HPSs manifest superior electrochemical properties as anode materials for LIBs. Importantly, this hybrid structure indicates a small irreversible capacity loss during the first discharge/charge cycle with a higher initial Coulombic efficiency of 77.3 wt%.

The $MFe_2O_4$@C HPSs composite was synthesized by simply carbonizing dual-functional heterometallic $Fe_2M$ clusters. As a precursor, taking the $Fe_2Co$ clusters as an example, the heterometallic $Fe_2Co$ clusters were first prepared as a microcrystalline product, and the structure of the clusters was identified by single-crystal X-ray diffraction (XRD) with a formula of $Fe^{III}_2Co^{II}O(CH_3COO)_6(H_2O)_3{\cdot}2H_2O$ according to previous report [29]. Briefly, the $Fe_2Co$ cluster is heterometallic mixed-valent complex with three metal centers arranging in the apex of an equilateral triangle (the middle image in Fig. 1), which is reinforced by one central O atom and six $CH_3COO^-$ ligands on three edges of triangle. Due to the imposed $D_{3h}$ molecular symmetry, Fe and Co atoms are indistinguishable in triangle but the atom ratio can be determined by inductively coupled plasma atomic emission spectroscopy (ICP-AES, Table S1 in Supporting information). In this structure, the total bond energies of metal and six oxygen coordination bonds should be higher than that of a single carbon-oxygen bond which will break easily. Finally, $CoFe_2O_4$@C HPSs formed in the calcination.

The phase composition and crystalline structure of the synthesized materials are depicted by X-ray diffraction (XRD) investigations. The XRD patterns of the $Fe_2M$ clusters were shown in Fig. S1 (Supporting information), which can be indexed to $Fe^{III}_2M^{II}O(CH_3COO)_6(H_2O)_3{\cdot}2H_2O$ without any impurity. After annealing treatment at 400 °C, the $Fe_2M$ clusters can be easily converted to $MFe_2O_4$@C HPSs (denoted as $MFe_2O_4$@C HPSs-400). Fig. 2a shows XRD patterns of $CoFe_2O_4$@C HPSs-400 and $CoFe_2O_4$@C HPSs-300. It is obviously that all the diffraction peaks assigned to cubic $CoFe_2O_4$ (JCPDS No. 03–0864), and no other peaks exist. In the $CoFe_2O_4$ crystal structure (Fig. 2b), all the tetrahedral sites were occupied by the Fe atom (marked by orange), and the octahedral sites were occupied by the Fe atom (marked by yellow) and Co atom (marked by blue), indicating the typical inverse spinel structure. By comparing the peak intensities, it found

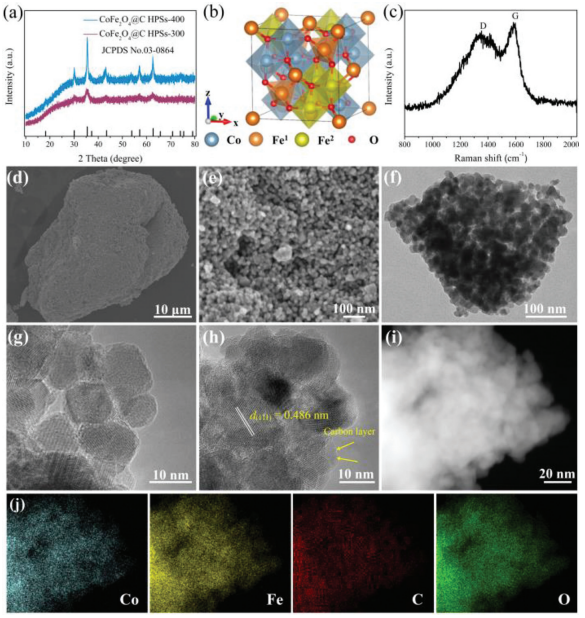


**Fig. 2.** (a) XRD patterns of the $CoFe_2O_4$@C HPSs. (b) Crystal structure of inverse spinel $CoFe_2O_4$. (c) Raman spectrum, (d,e) FESEM images, (f) TEM image and (g-i) HRTEM images of the $CoFe_2O_4$@C HPSs-400. (j) STEM-EDX element mappings of Co (blue), Fe (yellow), C (red) and O (green).

that the crystallinity of $CoFe_2O_4$@C HPSs-400 is better than that of $CoFe_2O_4$@C HPSs-300. The XRD patterns of $CoFe_2O_4$@C HPSs-500 (the $Fe_2Co$ heterometallic cluster calcined at 500 °C) was shown in Fig. S2 (Supporting information). It is clearly found that the cobalt metal obtained at 500 °C, indicating that a reduction reaction occurred. No diffraction peaks of carbon in $CoFe_2O_4$@C HPSs-400 were detected due to its amorphous feature. The Raman spectroscopy were further conducted to verify the porous carbon shell. As shown in Fig. 2c, the characteristic D and G peaks were located at 1347 and 1587 $cm^{-1}$, respectively. Generally, the $I_D/I_G$ ratio is used to evaluate the defects of carbon [30,31]. Here the $I_D/I_G$ is 0.804, indicating the porous carbon shell has more electroactive sites than graphite carbon, which is conducive to the diffusion of lithium-ion as well as beneficial to improving lithium storage performance [32].

The detailed morphology of the synthesized materials was investigated by scanning electron microscopy (SEM) and transmission electron microscopy (TEM). $Fe_2M$ clusters exhibited an irregular block with the relatively smooth surfaces (Fig. S3 in Supporting information). The $CoFe_2O_4$@C HPSs-400 had a morphology analogous to $Fe_2Co$ clusters (Fig. 2), although the surface becomes rough and the size is slightly reduced. As shown in Figs. 2d-f, the $CoFe_2O_4$@C HPSs-400 is composed of nanoparticles with the narrow size distribution at about 10 nm, and myriad mesopores from the assembly of nanoparticles are observable. The structure of the $CoFe_2O_4$@C HPSs-400 is further explored through typical TEM and high-resolution TEM (HRTEM) images. As shown in Figs. 2g and h, the nanoparticles are core-shell structures in which the core is coated by a porous carbon shell with a thickness of about 2–5 nm. The presence of the carbon layer plays an important role in the formation of $CoFe_2O_4$@C HPSs, because it can prevent the aggregation of $CoFe_2O_4$ particles and the formation of larger particles during high-temperature calcination. The carbon-containing composite obtained by calcining heterometallic clusters had a permeable structure, favorable for the rapid diffusion of electrolyte. Thermogravimetric analysis shows that the carbon content of $CoFe_2O_4$@C HPSs-400 is 5.3 wt% (Fig. S4 in Supporting information). Fig. 2h shows distinct lattice fringes with a distance of 0.486 nm corre-

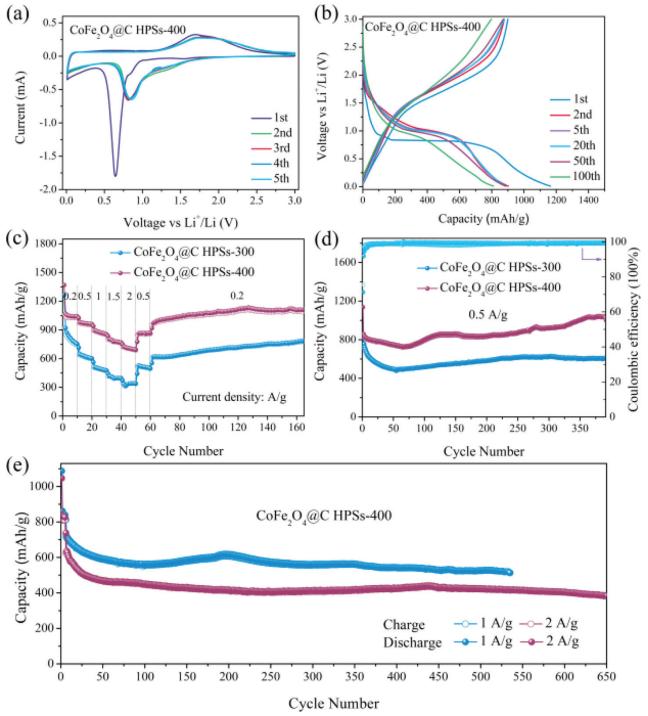


**Fig. 3.** Electrochemical performance of the $CoFe_2O_4$@C HPSs-400. (a) The first five CVs at a scan rate of 0.1 mV/s. (b) Galvanostatic charge/discharge profiles of the 1st, 2nd, 5th, 20th, 50th and 100th cycles at a current density of 0.2 A/g. (c) Rate capability at different current densities. Cycling performance at a current density of (d) 0.5 A/g, (e) 1 A/g and 2 A/g.

sponding to the (111) planes of $CoFe_2O_4$. Furthermore, scanning TEM (STEM) and energy-dispersive X-ray (EDX) elemental mappings are shown in Figs. 2i and j, indicating the Co, Fe, C and O are well distributed through the whole composites. The energy dispersive X-ray spectrum (EDX) revealed that the atomic ratio of Co to Fe is 1:2.07 (Fig. S5 in Supporting information). The ICP-AES further determined the molar ratio of Co to Fe to be 1:1.8 (Table S1 in Supporting information). The above results proved the successful preparation of $CoFe_2O_4$@C HPSs-400. The structure and composition characterization of $CoFe_2O_4$@C HPSs-400 were further examined by X-ray photo-electron spectroscopy (XPS) spectra and Brunauer-Emmett-Teller (BET) surface area (Fig. S6 in Supporting information). Interestingly, the same methodology can be applied to prepare other $MFe_2O_4$@C HPSs composite materials, such as $MnFe_2O_4$@C HPSs, $NiFe_2O_4$@C HPSs, $ZnFe_2O_4$@C HPSs, demonstrating the universality of the synthesis method. Correspondingly, $MnFe_2O_4$@C HPSs, $NiFe_2O_4$@C HPSs, $ZnFe_2O_4$@C HPSs have a similar structure to $CoFe_2O_4$@C HPSs, although they are slightly different in size and length. These differences in diameter and length are due to the different coordination reactions between metal ions and coordinating atoms which has a great influence on the nucleation and subsequent growth of the heterometallic cluster $Fe_2M$. The XRD patterns and SEM images of $MnFe_2O_4$@C HPSs, $NiFe_2O_4$@C HPSs and $ZnFe_2O_4$@C HPSs are shown in Fig. S7 (Supporting information).

The electrochemical properties of the as-prepared $CoFe_2O_4$@C HPSs are evaluated as anode materials for LIBs. The cyclic voltammogram (CV) curves of the $CoFe_2O_4$@C HPSs-400 for the first five cycles in the voltage range of 0.01–3.0 V at a scan rate of 0.1 mV/s are shown in Fig. 3a. During the first discharge scan, the peak centered at 0.64 V is attributed to the reduction reaction of $Fe^{3+}$ and $Co^{2+}$ to metallic Fe and Co, along with the formation of $Li_2O$ and solid electrolyte interface (SEI) films [33]. This cathodic peak shifts to 0.83 V in the subsequent cycles. The broad anodic peak at 1.23 V is associated with the oxidation of Fe and Co to $Fe_2O_3$ and CoO [34,35]. The electrochemical reaction can be expressed by the following equations:

$$CoFe_2O_4 + 8Li^+ + 8e^- \rightarrow Co + 2Fe + 4Li_2O \quad (1)$$

$$Co + 2Fe + 4Li_2O \rightarrow CoO + Fe_2O_3 + 8Li^+ + 8e^- \quad (2)$$

The difference between the peaks in the initial cycle and the successive cycles is assigned to the polarization processes of the electrode, which causes irreversible capacity loss in the first cycle [36,37]. Nevertheless, the CV curves are well overlapping except for the initial discharge, indicating the good reaction reversibility and structural stability of the $CoFe_2O_4$@C-400 HPSs. The representative galvanostatic charge-discharge voltage profiles of the $CoFe_2O_4$@C-400 HPSs at 0.2 A/g for different cycles are presented in Fig. 3b. The observed redox plateaus in the charge-discharge profiles match well with the CV curves. The voltage plateau of the first discharge curve at around 0.65 V can be attributable to the formation of SEI layers and the lithiation/delithiation reaction. The $CoFe_2O_4$@C HPSs-400 displays the initial discharge and charge capacities of 1164.2 and 899.7 mAh/g, respectively, corresponding to an initial Coulombic efficiency (CE) of 77.3%. The initial capacity loss can be ascribed to the irreversible formation of SEI films and irreversible insertion of the lithium ion into the $CoFe_2O_4$@C HPSs-400 [38]. In the subsequent cycles, the CE almost exceeds 90%, suggesting an improved cycling stability and reversibility.

Notably, the calcination temperature has a great influence on the electrochemical performance of the electrodes [39]. The rate capability and cycle stability of the $CoFe_2O_4$@C HPSs obtained at different calcination temperature are evaluated, as shown in Figs. 3c-e. The $CoFe_2O_4$@C HPSs-400 can deliver average capacities of 1045, 970, 878, 778 and 711 mAh/g at gradually increasing current densities of 0.2, 0.5, 1.0, 1.5 and 2.0 A/g, respectively, much better than $CoFe_2O_4$@C HPSs-300 (Fig. 3c). The high performance of the $CoFe_2O_4$@C HPSs-400 can be ascribed to the highly crystalline than that of $CoFe_2O_4$@C HPSs-300. More importantly, the larger specific surface area of the $CoFe_2O_4$@C HPSs-400 can make the electrode and electrolyte contact better and improve the lithium storage efficiency during lithium intercalation/deintercalation process. Even when the current density returns to 0.5 A/g and 0.2 A/g, the specific capacity of $CoFe_2O_4$@C HPSs-400 can still reach 868 and 1135 mAh/g, revealing the excellent structural stability of the $CoFe_2O_4$@C HPSs-400. The cycling stability of $CoFe_2O_4$@C HPSs-400 and $CoFe_2O_4$@C HPSs-300 were compared at the current density of 0.5 A/g (Fig. 3d). $CoFe_2O_4$@C HPSs-400 displays prominent cycling stability with the specific capacity of 1040 mAh/g after 390 cycles, while the specific capacity of the $CoFe_2O_4$@C HPSs-300 is only 608 mAh/g. The long-term cycling stability of $CoFe_2O_4$@C HPSs-400 at a current density of 1 A/g and 2 A/g are further evaluated. As shown in Fig. 3e, the $CoFe_2O_4$@C HPSs-400 anode exhibited a specific capacity of 520 mAh/g after 530 cycles at 1 A/g and still maintains at 390 mAh/g at 2 A/g after 650 cycles, indicating the excellent structure robustness. Postmortem study shows that the shape and structural integrity of the $CoFe_2O_4$@C HPSs-400 can be well retained after 50 cycles (Fig. S8 in Supporting information). The outstanding performance of the $CoFe_2O_4$@C HPSs-400 might be attributed to the unique structural and compositional features. To be specific, the construction of $CoFe_2O_4$ nanoparticle and carbon subunits not only enables a short diffusion distance for fast diffusion of Li ions but also provides sufficient contact between active material and electrolyte for the rapid charge-transfer reaction. Moreover, the carbon coated secondary $CoFe_2O_4$ nanoparticles can effectively withstand large volume variation upon cycling, therefore maintaining structural integrity. In addition, the carbon shell can enhance the electronic conductivity thus improving the rate capability, as well as

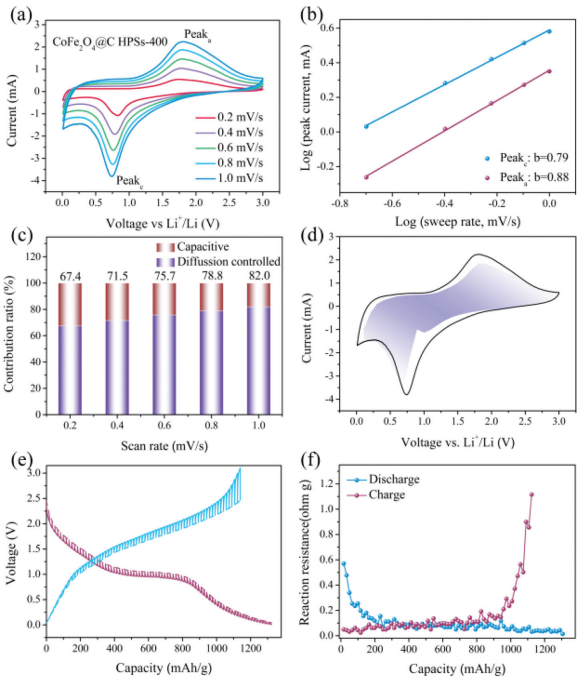


**Fig. 4.** Kinetics analysis of the $CoFe_2O_4$@C HPSs-400 electrode. (a) CV curves of the fresh cells at various scan rates. (b) *b*-value analysis using the relationship between the peak currents and scan rates. (c) Contribution ratio of the capacitive and diffusion-controlled charges at different scan rates. (d) Separation of the capacitive (purple region) and diffusion currents at a scan rate of 1.0 mV/s. (e) GITT voltage profiles. (f) Reaction resistance in discharge and charge process, respectively.

the electrochemical reactivity further improving the electrochemical property. In the meanwhile, the electrochemical performance of $MnFe_2O_4$@C HPSs, $NiFe_2O_4$@C HPSs, and $ZnFe_2O_4$@C HPSs are also studied. As shown in Figs. S9-S11 (Supporting information), these $MFe_2O_4$@C HPSs show high specific capacities, enhanced cycling durability and good rate tolerance as anodes for LIBs. The performances of $MFe_2O_4$@C HPSs are evaluated by comparison with other related reports as anode materials of LIBs in Table S2 (Supporting information), suggesting the superior electrochemistry behaviors of the $MFe_2O_4$@C HPSs in this works.

To comprehensively explore the electrochemical reaction kinetics of $CoFe_2O_4$@C HPSs-400 electrode, the CV curves at different scan rates from 0.2 mV/s to 1.0 mV/s were performed, as shown in Fig. 4a. In general, the peak current ($i$) and scan rate ($v$) obey the following relationship [40-42]: $\log i = \log a + b\log v$, where $a$ and $b$ are fitting parameters. The $b$ value can be obtained from the slope of the plot of $\log i$ *versus* $\log v$. The Li storage mechanism is determined by the $b$ value. $b = 0.5$ represents that the electrochemical process is diffusion-controlled while 1.0 means capacitive-controlled process. As shown in Fig. 4b, the calculated $b$ values are 0.79 and 0.88 for the reduction and the oxidation peaks, respectively, indicating the mixed process dominated by both diffusion-controlled and capacitive-controlled process. The ratio of the contributions from the capacitive contribution ($k_1v$) and diffusion-controlled contribution ($k_2v^{1/2}$) at a fixed potential (V) can be quantified by the following formula [40]: $i = k_1v + k_2v^{1/2}$, where $k_1$ and $k_2$ are constant parameters. As shown in Fig. 4c, the capacitive contribution grows progressively as a function of the scan rate, so that it achieves a maximum value of 82% at 1 mV/s in Fig. 4d. Thus, it is demonstrated that the majority mechanism of Li storage in $CoFe_2O_4$@C HPSs-400 electrode is in line with the capacitive-controlled processes, which greatly contributes to the high-rate capability. The capacitance dominant process can be mainly derived from the structural superiority of $CoFe_2O_4$@C HPSs-400 composite, in which nanosized $CoFe_2O_4$ can offer reduced diffusion pathways for both lithium ions and electrons while the carbon coating affords superior electrolyte accessibility to the electrochemically active $CoFe_2O_4$ nanoparticles, accounting for excellent electrochemical performances [43].

To further interpret the diffusivity of active lithium species in $CoFe_2O_4$@C HPSs-400 during the charge/discharge process, galvanostatic intermittent titration technique (GITT) and electrochemical impedance spectroscopy (EIS) were conducted. GITT curves of $CoFe_2O_4$@C HPSs-400 are shown in Fig. 4e, in which the dotted lines showed the quasi equilibrium open-circuit-voltages (OCVs). The internal resistance is derived from dividing the voltages difference between the OCVs and the closed circuit voltages (CCVs) by the pulse current [44]. The internal resistance changes of $CoFe_2O_4$@C HPSs-400 in the charge/discharge process were shown in Fig. 4f. It can be seen that the internal resistance in the discharge process decreased gradually, which can be ascribed to that the formation of metals or intermetallics enhanced the electronic conductivity and the immersion of the electrolyte accelerated the migration ions. Upon charge, there is a gradually increase of the internal resistance along with the release of lithium ions, which is contrary to the discussion above. The enhanced diffusion kinetics of $CoFe_2O_4$@C HPSs-400 can also be verified by EIS (Fig. S12 in Supporting information). The Nyquist plots of the $CoFe_2O_4$@C HPSs-400 electrode are constituted of the semicircle at the high frequencies (charge-transfer resistance, $R_{ct}$) and the slope of the line at the low-frequencies (Warburg impedance $R_w$). The $R_{ct}$ of the $CoFe_2O_4$@C HPSs-400 electrode after the 50 cycles was evidently smaller than that after the first cycle, which confirms the remarkably accelerated reaction kinetics upon cycles. The boosted diffusion coefficient of Li ion resulted from the hierarchical structure with mesoporous and the presence of the carbon shell.

Through a one-step method, a controlled synthesis of the carbon shell-encapsulated $MFe_2O_4$ composites was achieved. That's to say, the bifunctional heterometallic $Fe_2M$ cluster was calcined to obtain the final product $MFe_2O_4$@C HPSs, including $CoFe_2O_4$@C HPSs, $MnFe_2O_4$@C HPSs, $NiFe_2O_4$@C HPSs and $ZnFe_2O_4$@C HPSs. This method is very versatile and has the potential to be further extended to other materials. The prepared $MFe_2O_4$@C HPSs showed excellent lithium storage performance as an anode material. The $CoFe_2O_4$@C HPSs-400 remains 1040 mAh/g after 390 cycles at a current density of 0.5 A/g and 520 mAh/g after 530 cycles at a current density of 1 A/g. This work not only makes a significant contribution to the synthesis methodology of novel composite structure, but also to the application of transition metal oxides as negative electrodes of lithium ion batteries.

## Declaration of competing interest

The authors declare that they have no known competing financial interests or personal relationships that could have appeared to influence the work reported in this paper.

## Acknowledgments

The authors gratefully acknowledge the financial support provided by the National Natural Science Foundation of China (No. 21871164), the Taishan Scholar Project Foundation of Shandong Province (No. ts20190908), the Natural Science Foundation of Shandong Province (No. ZR2019MB024), the China Postdoctoral Science Foundation (No. 2018M632666), and the Special Fund for Postdoctoral Innovation Program of Shandong Province (No. 201901003).

## Supplementary materials

Supplementary material associated with this article can be found, in the online version, at doi:10.1016/j.cclet.2021.06.074.

## References


[1] T. He, J. Feng, Y. Zhang, et al., Adv. Energy Mater. 8 (2018) 1702805.
[2] Y. Chiang, Science 330 (2010) 1485–1486.
[3] T. He, J. Feng, J. Ru, et al., ACS Nano 13 (2019) 830–838.
[4] P. Simon, Y. Gogotsi, Nat. Mater. 7 (2008) 845–854.
[5] C. Lee, S.D. Seo, D. Kim, et al., Nano Res. 6 (2013) 348–355.
[6] C. Morales-Guio, S. Tilley, H. Vrubel, et al., Nat. Commun. 5 (2014) 3059.
[7] C. Hao, T. Gao, A. Yuan, et al., Chin. Chem. Lett. 32 (2021) 113–118.
[8] Y. Li, Y. Xu, W. Yang, et al., Small 14 (2018) 1704435.
[9] Y. Li, X. Han, T. Yi, et al., J. Energy Chem. 31 (2019) 54–78.
[10] L. Zhang, T. Wei, Z. Jiang, et al., Nano Energy 48 (2018) 238–247.
[11] G. Zeng, N. Shi, M. Hess, et al., ACS Nano 9 (2015) 4227–4235.
[12] K. Wu, D. Liu, Y. Tang, et al., Electrochim. Acta 263 (2018) 515–523.
[13] Z. Zhang, Y. Wang, M. Zhang, et al., J. Mater. Chem. A 1 (2013) 7444–7450.
[14] M. Lu, H. Li, W. Han, et al., Nanoscale 11 (2019) 15037–15042.
[15] H. Tong, C. Wang, J. Lu, et al., Small 16 (2020) 2002771.
[16] G. Ma, C. Li, F. Liu, et al., Mater. Today Energy 10 (2018) 241–248.
[17] T. Shimizu, H. Wang, D. Matsumura, et al., ChemSusChem 13 (2020) 2256–2263.
[18] S. Tao, P. Cui, S. Cong, et al., Sci. China Mater. 63 (2020) 1672–1682.
[19] M. Huang, K. Mi, J. Zhang, et al., J. Mater. Chem. A 5 (2017) 266–274.
[20] X. Cao, B. Zheng, W. Shi, et al., Adv. Mater. 27 (2015) 4695–4701.
[21] Y. Chen, L. Yu, X.W. Lou, Angew. Chem. Int. Ed. 55 (2016) 5990–5993.
[22] R. Wu, D. Wang, X. Rui, et al., Adv. Mater. 27 (2015) 3038–3044.
[23] F. Cao, M. Zhao, Y. Yu, et al., J. Am. Chem. Soc. 138 (2016) 6924–6927.
[24] Y. Cai, G. Fang, J. Zhou, et al., Nano Res. 11 (2018) 449–463.
[25] A. Tayi, A. Shveyd, A. Sue, Nature 488 (2012) 485–489.
[26] S. Wang, S. Jin, S. Yang, et al., Sci. Adv. 1 (2015) e1500441.
[27] J. Jia, Q. Wang, J. Am. Chem. Soc. 131 (2009) 16634–16635.
[28] H. Yang, Y. Wang, H. Huang, et al., Nat. Commun. 4 (2013) 2422.
[29] H. Jang, K. Kaji, M. Sorai, et al., Inorg. Chem. 29 (1990) 3547–3556.
[30] P. Lu, Y. Sun, H. Xiang, et al., Adv. Energy Mater. 8 (2018) 1702434.
[31] K. Wang, Z. Lu, Y. Li, et al., ChemSusChem 13 (2020) 5539–5548.
[32] H. Wang, Z. Cui, C. Fan, et al., Chem. Eur. J. 24 (2018) 6798–6803.
[33] J. He, Y. Chen, P. Li, Electrochim. Acta 182 (2015) 424–429.
[34] M. Zhang, X. Yang, X. Kan, et al., Electrochim. Acta 112 (2013) 727–734.
[35] X. Sun, X. Zhu, X. Yang, et al., Green Energy Environ. 2 (2017) 160–167.
[36] L. Yao, H. Deng, Q. Huang, et al., J. Alloy. Compd. 693 (2017) 929–935.
[37] W. Shi, J. Zhu, X. Rui, et al., ACS Appl. Mater. Interfaces 4 (2012) 2999–3006.
[38] Q. Peng, S. Zhang, H. Yang, et al., ACS Nano 14 (2020) 6024–6033.
[39] N. Wang, H. Xu, L. Chen, et al., J. Power Sources 247 (2014) 163–169.
[40] X. Zhao, Y. Wu, Y. Wang, et al., Nano Res. 13 (2020) 1044–1052.
[41] Y. Chu, B. Xi, S. Xiong, Chin. Chem. Lett. 32 (2021) 1983–1987.
[42] Z. Zheng, H. Wu, H. Liu, et al., ACS Nano 14 (2020) 9545–9561.
[43] J. Tang, X. Huang, T. Lin, et al., Energy Storage Mater. 26 (2020) 550–559.
[44] S. Kim, M. Kim, S. Choi, et al., Energy Environ. Sci. 8 (2015) 1538–1543.